Energy Engineering

Tech Science Press

http://doi.org/10.32604/ee.2026.088425

ARTICLE

Study on the Erosion Characteristics of Flow-Passage Components in the Jet Mechanism of an Impulse Turbine

Shurong Feng[1], Dongping Zeng[1,2,3,*], Xingyan Chen[2], Yanan Zhao[1] and Fada Zhou[2]

[1]Power China Zhongnan Engineering Corporation Limited, Changsha, China
[2]School of Energy and Power Engineering, Changsha University of Science and Technology, Changsha, China
[3]School of Hydraulic and Ocean Engineering, Changsha University of Science and Technology, Changsha, China
*Corresponding Author: Dongping Zeng. Email: zengdp@csust.edu.cn

Received: 03 July 2026; Accepted: 31 July 2026; Published: 12 November 2026

ABSTRACT: Under China's "Dual Carbon" strategy, which directs hydropower development toward the high-head regions of the southwest, impulse turbines have become the main turbine type for exploiting high-head hydropower resources. During the flood season, the high sediment loads carried by rivers in the southwest cause severe erosion of the jet mechanism, posing a significant threat to the safe and stable operation of the units. Taking a single jet mechanism of a six-nozzle impulse turbine at a hydropower station as the study object, a three-dimensional computational model covering the jet flow region was established. The renormalization group (RNG) k-ε turbulence model, the volume of fluid (VOF) multiphase model, and the Euler–Lagrange discrete phase model (DPM) were combined with the Oka erosion model to systematically investigate the effects of sediment particle diameter, volume fraction, and needle opening on the erosion characteristics of the nozzle and the jet needle. The results show that as the sediment particle diameter increases, the eroded area on the jet needle extends towards the shank, whereas erosion of the nozzle first increases, then drops sharply, and finally recovers gradually. The sediment volume fraction is positively correlated with the erosion rate, and this dependence is approximately exponential rather than linear; under the same operating conditions, the erosion of the jet needle is consistently greater than that of the nozzle. The needle opening is negatively correlated with the total erosion: erosion is most severe at small openings and decreases as the opening increases. When the needle opening increases from 0.23 to 0.63, the maximum erosion rate of the jet needle decreases by about 99.8%. This study identifies the high-erosion-risk regions and the main influencing factors in the jet mechanism of impulse turbines, providing a theoretical basis for the erosion-resistant design of the jet mechanism and for the formulation of operation and maintenance strategies for the units.

KEYWORDS: Impulse turbine; sediment particle size; water–air–sediment three-phase flow; erosion characteristics; numerical simulation

1 Introduction

Under China's "Dual Carbon" strategy, hydropower development is increasingly concentrated in the high-head regions of the southwest, where impulse turbines have become the dominant choice owing to their suitability for high heads and wide efficient operating ranges [1]. However, rivers in this region carry heavy sediment loads during flood seasons. Driven by high-speed jets, sediment particles continuously erode the flow-passage components, particularly the nozzle and jet needle of the jet mechanism, degrading jet quality and reducing turbine output [2–5]. Therefore, understanding the erosion characteristics of the jet mechanism under sediment-laden flow is of great significance.

Copyright © 2027 The Authors. Published by Tech Science Press. This work is licensed under a Creative Commons Attribution 4.0 International License, which permits unrestricted use, distribution, and reproduction in any medium, provided the original work is properly cited.

Extensive research has been devoted to sediment erosion in impulse turbines. In terms of numerical methodology, Sun et al. [6] compared different runner-rotation modeling strategies and their effects on erosion prediction. Regarding sediment particle size and concentration, Rai et al. [7] experimentally quantified the power-law dependence of bucket erosion on these factors; Ge et al. [8] simulated sediment flow in the distribution pipe and proposed optimized sand-outlet geometries that reduced nozzle abrasion by over 50%; Guo et al. [9] revealed non-uniform erosion among injectors due to upstream flow asymmetry; Song et al. [10] linked finer particles to higher erosion and entropy generation. Concerning needle opening, Sun et al. [11] developed a risk-assessment framework and found that erosion increases with opening; Li et al. [12] showed that increasing the needle angle can reduce tip erosion by up to 94%, though with hydraulic penalties. Regarding geometric parameters, Li et al. [13] demonstrated that nozzle angle and needle transition geometry significantly affect erosion distribution. Additionally, erosion-induced mass loss has been shown to influence runner natural frequencies and transient stresses [14,15]. Collectively, this body of work has established the Computational Fluid Dynamics (CFD) framework for hydro-abrasive erosion prediction in impulse turbines and has quantified how sediment concentration and particle size govern the erosion rate.

Despite these efforts, most existing studies focus on one or two factors and predominantly on the runner or buckets, leaving a systematic comparison of particle diameter, sediment concentration, and needle opening within a unified jet-mechanism model still lacking. This study fills this gap by numerically simulating the water–air–sediment three-phase flow in a single jet mechanism using the RNG k-ε turbulence model, Euler–Lagrange particle tracking, and the Oka erosion model. We systematically investigate the effects of the three parameters on erosion magnitude and distribution on both the nozzle and the jet needle, and combine the results with particle-trajectory analysis to reveal the underlying mechanisms. The findings provide a theoretical basis for erosion-resistant design and operation-maintenance strategies. Limitations include the use of monodisperse spherical particles, one-way coupling, constant inlet velocity, and lack of quantitative experimental validation.

2 Computational Model and Verification

2.1 Turbulence Models and Control Equations

In this study, Fluent was used to perform numerical simulations of the water–air–sediment three-phase flow (where the water-gas interface is captured using the VOF method, and sediment particles are tracked via the Euler-Lagrange DPM method) in the jet mechanism of the impulse turbine. The RNG k-ε turbulence model was used to describe the flow of the continuous phase, while the Euler–Lagrange discrete phase model (DPM) was used to track the trajectories of the sediment particles. In addition, the Oka erosion model was used to predict the sediment erosion within the jet mechanism. The governing equations of each model are given as follows:

The RNG k-ε turbulence model improves upon the standard k-ε model and is more suitable for flows with high strain rates and swirl. Its two principal advantages over the standard k-ε model are that its coefficients are derived analytically from renormalization-group theory rather than being calibrated empirically, and that an additional strain-rate term in the ε equation allows it to respond to rapid straining and streamline curvature [16]. This makes it well suited to the strongly accelerating, swirling flow through the nozzle contraction and the shear layer of the free jet studied here; the same turbulence model was also adopted in the validation benchmark of Ge et al. [5], where it was successfully validated for similar confined

swirling flows, and in similar jet-mechanism erosion studies [13], which facilitates direct comparison. The transport equations for the turbulent kinetic energy k and the dissipation rate ε are given by [16]:

$$\frac{\partial k}{\partial t} + U_j \frac{\partial k}{\partial x_j} = \frac{\partial}{\partial x_j}\left[(\nu + \alpha_k \nu_t)\frac{\partial k}{\partial x_j}\right] + G_k + G_b - \varepsilon - Y_M + S_k \tag{1}$$

$$\frac{\partial \varepsilon}{\partial t} + U_j \frac{\partial \varepsilon}{\partial x_j} = \frac{\partial}{\partial x_j}\left[(\nu + \alpha_\varepsilon \nu_t)\frac{\partial \varepsilon}{\partial x_j}\right] + C_{1\varepsilon}\frac{\varepsilon}{k}(G_k + C_{3\varepsilon}G_b) - C_{2\varepsilon}\frac{\varepsilon^2}{k} - R_\varepsilon + S_\varepsilon \tag{2}$$

In the equation, v_t represents the turbulent viscosity, R_ε is the strain-rate correction term, and the remaining symbols are standard constants of the RNG k-ε model. The discrete phase model in Fluent was used to simulate the motion of the sediment particles in the fluid [17].

$$\frac{du_p}{dt} = \frac{18\mu}{\rho_p d_p^2}\frac{C_D Re}{24}(u - u_p) + \frac{g_y(\rho_p - \rho)}{\rho_p} + F_x \tag{3}$$

In the equation, u is the fluid-phase velocity (m/s); u_p is the particle velocity (m/s); μ is the dynamic viscosity (Pa·s); ρ_p is the particle density, kg/m^3; d_p is the particle diameter, m; C_D is the drag coefficient, calculated as a function of the particle Reynolds number Re using the Schiller–Naumann correlation, which is applicable to spherical particles [18].

The erosion of the wall surfaces caused by sediment particles is predicted using the Oka model, which accounts for factors such as particle diameter, impact velocity, impact angle, and material hardness. The erosion function is [13,19,20]:

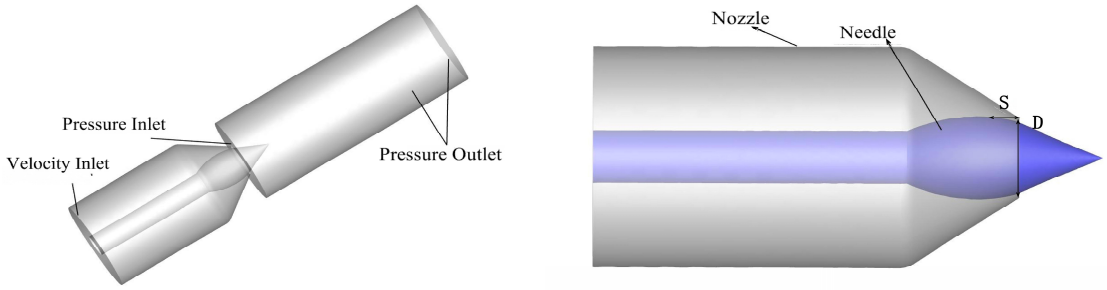
$$E(\alpha) = g(\alpha)E_{90} \tag{4}$$

$$g(\alpha) = (\sin(\alpha))^{\eta_1}(1 + Hv(1 - \sin(\alpha)))^{\eta_2} \tag{5}$$

In the equation, E_{90} is the reference erosion rate for a 90° perpendicular impact. H_V is the Vickers hardness of the wall material. For austenitic stainless steel, the common base material of hydraulic turbines, this value is taken as 1.83 GPa. η_1 and η_2 are constants of the impact angle function [13].

2.2 Model of the Jet Mechanism for an Impulse Turbine

This paper studies the jet mechanism of a six-nozzle impulse turbine at a hydropower station. A three-dimensional model of the jet mechanism of the impulse turbine was built in SolidWorks; Fig. 1a shows the computational domain of a single jet mechanism. The jet mechanism consists of a jet needle and a nozzle. When defining the computational domain, the jet flow region was extended beyond the nozzle outlet, with a length of 3D and a width of 7D, in order to observe the jet behavior in the free-flow region. Specifically, the length of 3D and width of 7D were chosen so that the free jet develops fully before reaching the outlet boundary of the computational domain and so that the lateral boundaries remain well away from the jet core and its entrainment region, thereby avoiding spurious boundary reflection; this domain size is consistent with the validation benchmark of Ge et al. [5] and with the similar jet-mechanism configuration adopted by Li et al. [13]. In addition, the needle opening is denoted by SR and defined as SR = S/D, where S is the needle stroke and D is the nozzle outlet diameter, as shown in Fig. 1b.



(**a**) Boundary Conditions (**b**) Jet Mechanism

Figure 1: Calculation model of single jet mechanism. Abbreviations: S: needle stroke (m); D: nozzle outlet diameter (m).

Water and air were treated as continuous phases, and a three-dimensional transient simulation of the water–air two-phase flow was carried out with a time step of 0.005 s. An implicit VOF formulation together with an implicit body-force scheme was adopted, which permits a global Courant number greater than one; this setup, including the 0.005 s time step, follows the validation benchmark of Ge et al. [5], who performed an unsteady three-phase (water–air–sediment) simulation of the same six-nozzle jet-mechanism model, and was confirmed in the present study to give well-converged residuals at an acceptable computational cost for the three-phase transient simulation. The RNG k-ε turbulence model was used, with the VOF model enabled to capture the interface; an implicit scheme was adopted, and the implicit body-force formulation was used to balance the pressure gradient and the body forces in the momentum equations, thereby improving the convergence of the solution. The Semi-Implicit Method for Pressure-Linked Equations–Consistent (SIMPLEC) algorithm was used for the pressure–velocity coupling, and a first-order upwind scheme was selected for the spatial discretization. A momentum under-relaxation factor of 0.2 was used to improve the convergence of the continuity-phase residual, with the other relaxation factors kept at their default values; in addition, because the Froude and Weber numbers of the unsteady flow are both large, the influence of gravity and surface tension on the main flow characteristics is small, and these effects were therefore neglected in the calculation, consistent with the validation benchmark of Ge et al. [5]. The water inlet boundary was set as a velocity inlet with a velocity of 0.857 m/s; the air inlet boundary was set as a pressure inlet with a relative pressure of 0 Pa; and the outlet was set as a pressure outlet with a relative pressure of 0 Pa. Because the jet discharged by the jet mechanism of an impulse turbine flows directly into the atmosphere, both the air inlet and the outlet are open to the ambient air; the reference pressure was therefore taken as the local atmospheric pressure, i.e., a relative (gauge) pressure of 0 Pa, consistent with the actual operating environment of the unit. The sediment inlet boundary was also set as a velocity inlet, with the same velocity as the clear water. After the water–air two-phase flow had fully converged and the flow field had stabilized, sediment particles (default spherical shape) were added; the injection type was set to ‘surface’ with the injection direction normal to the surface, and a transient simulation of the water–air–sediment three-phase flow was then performed. It should be noted that this study adopts a constant inlet velocity condition. The erosion variation with needle opening includes the combined effect of flow passage geometry and flow rate change.

The sediment particles are represented as spheres, which is the standard treatment in Euler–Lagrange discrete-phase simulations and allows the effect of particle diameter to be isolated using a single characteristic length; the same assumption has been adopted in similar Pelton/impulse-turbine erosion studies [7,13,20]. Natural sediment particles are generally non-spherical and cover a range of sizes; such irregularity would

be expected to influence the results mainly through an additional shape factor in the drag and erosion calculations, which generally tends to increase the predicted erosion to some extent. The effects of particle shape and of the real particle-size gradation are therefore identified as a limitation of the present study.

It should be noted that the present study is based on a reduced-scale model of an impulse turbine, following the geometry and operating conditions of Ge et al. [5]. The inlet velocity of 0.857 m/s is the model inlet value determined from the corresponding model experiment. Owing to the strong contraction of the flow passage, the flow accelerates markedly downstream, and the jet velocity at the nozzle outlet reaches about 32 m/s, which is consistent with the high-speed jet of an impulse turbine; the static pressure simultaneously drops from about 563 kPa (area-weighted average) at the inlet to a slightly negative value near the nozzle outlet, indicating that most of the pressure energy is converted into kinetic energy there. Together with the mesh-independence verification presented in Section 2.3, these geometric, boundary-condition, and numerical-scheme settings jointly underpin the numerical stability and reliability of the simulations.

2.3 Mesh Generation and Grid-Independence Verification

Fig. 2 shows the fluid-domain mesh of the jet mechanism model of the impulse turbine. A polyhedral mesh was used to discretize the jet needle, the nozzle, and the jet flow region of the complete flow-passage model, with refined boundary layers in the fluid regions near the jet needle and the nozzle. To further reduce the numerical error, the ratio of the actual jet velocity at the nozzle outlet to the theoretical velocity (velocity coefficient C_V) was used as a performance indicator of the jet to verify grid independence. As shown in Fig. 3, five mesh models with different densities were generated for the jet mechanism. When the number of mesh elements increased from 1.37 million to 1.59 million, C_V increased markedly; however, a further increase from 1.59 million to 2.5 million yielded only a marginal change in the performance of the jet mechanism. Taking both computational efficiency and mesh quality into account, 1.59 million elements were finally selected for the numerical simulation.

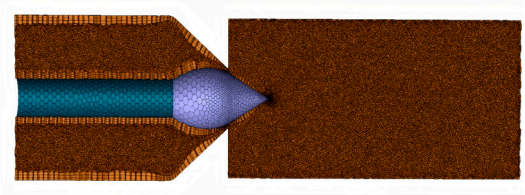


Figure 2: Schematic diagram of the full jet mechanism grid.

To further verify the reliability of the present model, the simulated flow field was compared with the published results of Ge et al. [5], who investigated the same six-nozzle jet-mechanism model under the same operating conditions (design head 32 m, design flow rate 0.038 m^3/s, nozzle-inlet diameter 125 mm, and inlet velocity 0.857 m/s). As shown in Fig. 3b, the maximum nozzle-outlet jet velocity obtained in this study (about 32.5 m/s) and the area-weighted average nozzle-inlet pressure (about 563 kPa) agree well with the values reported by Ge et al. [5] (36 m/s and 566 kPa), the relative differences being 9.7% and 0.5%, respectively; both studies also predict a slightly negative pressure near the nozzle outlet, confirming that most of the pressure energy is converted into kinetic energy. The somewhat larger difference in the jet velocity is likely attributable to the numerical dissipation introduced by the first-order upwind scheme, which tends to reduce the predicted peak jet velocity, together with differences in mesh resolution and in the capture of the VOF interface within the narrow annular gap, and in the sampling of instantaneous

versus statistically averaged values, relative to the results of Ge et al. [5], as well as in solver settings between the two studies. By contrast, the area-weighted inlet pressure differs by only 0.5% between the two studies, indicating that the overall energy conversion is consistent and that the discrepancy is concentrated in this one local, peak-velocity quantity; a cross-check using a second-order discretization scheme and/or a further-refined mesh has been identified as a topic for future work. In terms of the erosion distribution, the high-erosion zones predicted in this study, located at the jet-needle tip and on the annular inner wall near the nozzle outlet, are qualitatively consistent with the field erosion survey of Bajracharya et al. [2] and with the numerical results of Li et al. [13] obtained using the same VOF–Euler–Lagrange–Oka approach. These comparisons, covering both the flow field and the erosion distribution, indicate that the present model reproduces the dominant flow and erosion characteristics of the jet mechanism with acceptable accuracy. In addition, the trend of increasing erosion with increasing sediment concentration and particle diameter obtained in this study is consistent with the experimental observations of Rai et al. [7]. Owing to the lack of quantitative erosion-experiment data obtained under exactly matching operating conditions, direct quantitative validation of the predicted erosion rates is identified as a topic for future work; the present validation therefore relies on qualitative and trend-level agreement with the flow-field, field-survey, and numerical evidence discussed above.

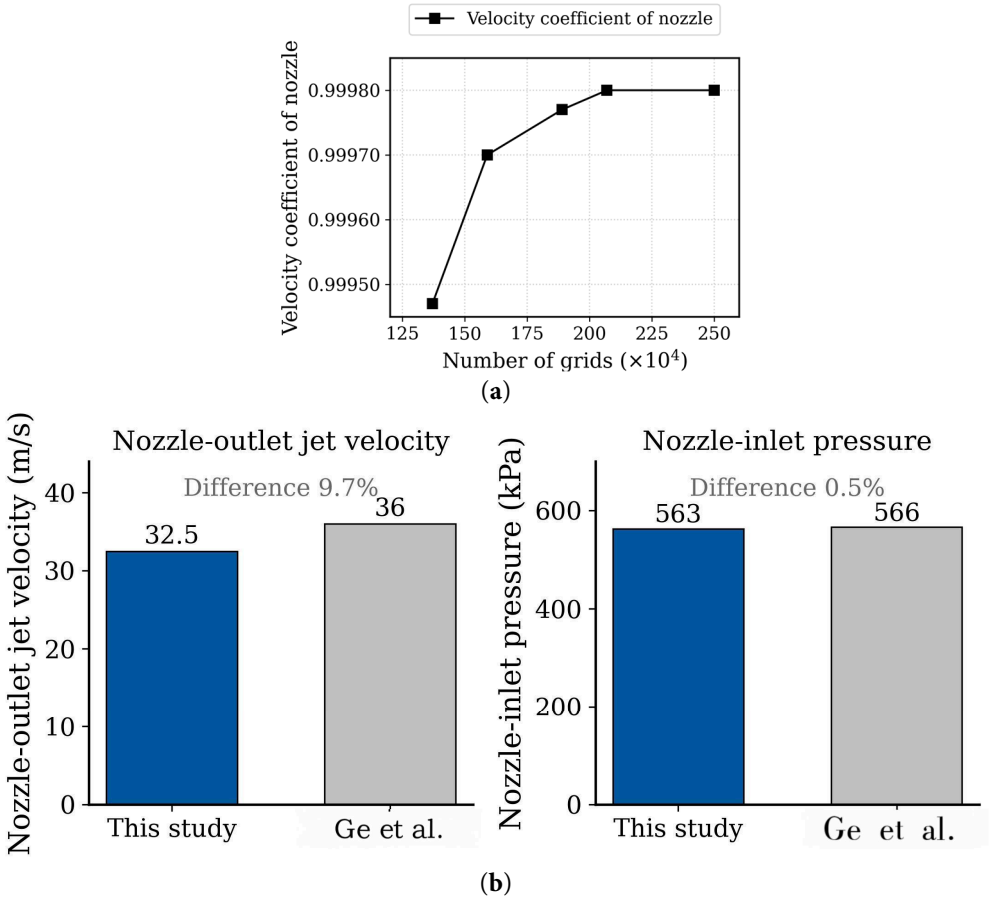
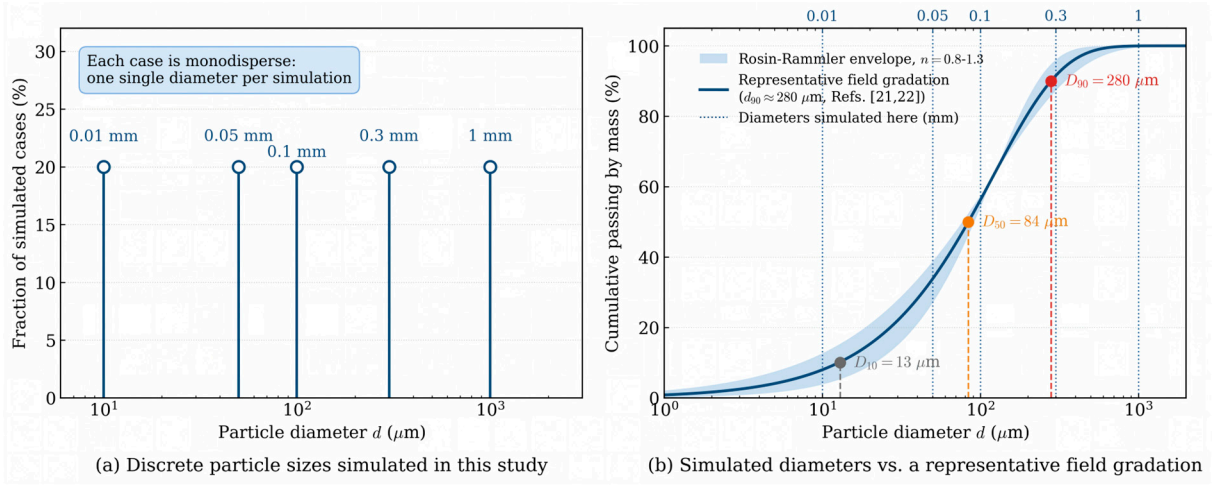


Figure 3: Verification of the numerical model. (**a**) nozzle velocity coefficient versus number of grids; (**b**) comparison of the flow-field results with Ge et al. [5].

It should also be noted that the constants used in the Oka erosion model, including H_V = 1.83 GPa for austenitic stainless steel, were taken from the calibration reported in the original Oka model references [19,20]. The absolute erosion rate predicted by the model is sensitive to the specific values of these constants; however, the present study focuses on the relative trends and distribution patterns of erosion among the three parameters investigated, which are particle diameter, sediment volume fraction, and needle opening, and these relative trends are not expected to change with a rescaling of the model constants.

Fig. 4a shows the five discrete particle diameters simulated in this study (0.01, 0.05, 0.1, 0.3, and 1 mm). We note that each simulation case is monodisperse, i.e., a single uniform diameter is used per simulation, rather than a polydisperse mixture; the five sizes therefore appear as discrete spikes, each representing 20% of the simulated cases, rather than as a continuous distribution.

Fig. 4b places these simulated diameters in the context of a representative field particle size distribution. The cumulative passing curve corresponds to a representative field gradation reported by Vishwakarma and Pant [21] and Wei et al. [22], and is well described by a Rosin–Rammler distribution with a spread parameter of $n \approx 1.0$; the shaded band shows the envelope for n = 0.8–1.3, covering the typical variability of field materials. The vertical dotted lines mark the five diameters simulated here. As can be seen, the selected sizes span the full range of the field gradation from below D10 to well above D90, so that the parametric study on monodisperse cases brackets the particle sizes encountered in practice.



(a) Discrete particle sizes simulated in this study (b) Simulated diameters vs. a representative field gradation

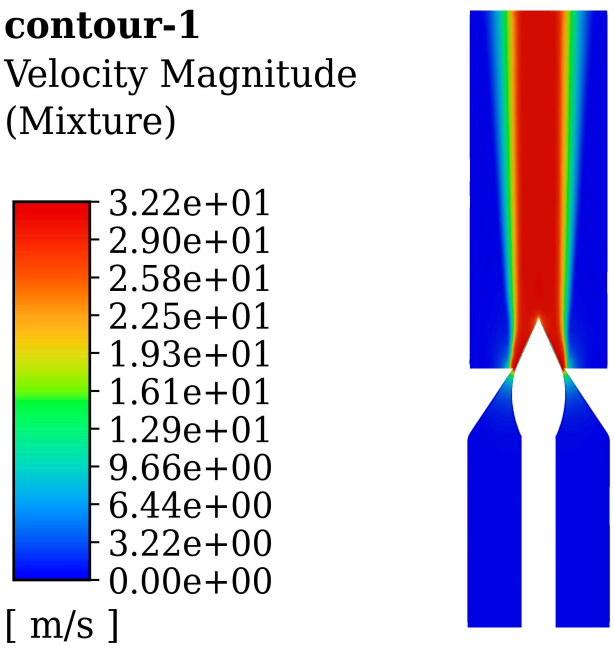
Figure 4: Particle sizes simulated in this study and a representative field particle size distribution.

3 Results and Discussion

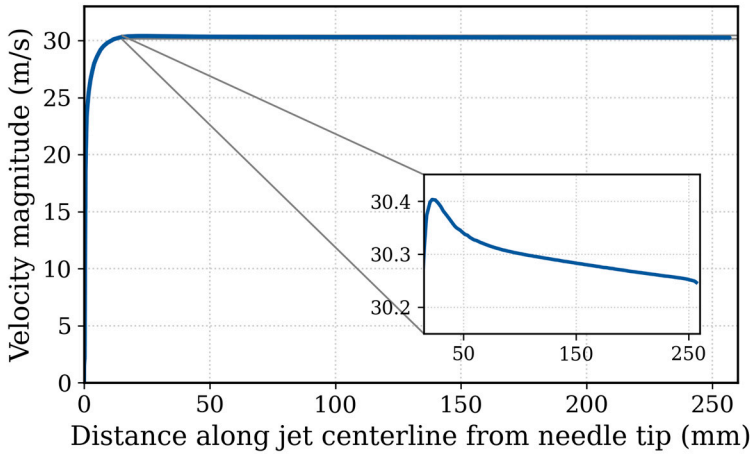
3.1 Flow Field Characteristics of the Jet Mechanism

Before analyzing the erosion, the base water–air flow field of the jet mechanism (without sediment) is examined. Because the discrete phase is one-way coupled to the continuous phase, this flow field applies to all the sediment cases considered in the following sections.

Fig. 5 shows the velocity field of the jet mechanism. The flow accelerates continuously through the nozzle contraction and reaches its maximum (about 32.5 m/s) in the annular gap between the jet needle and the nozzle and at the needle tip, where the jet is formed. This high-velocity region coincides with the severely eroded zones identified below, indicating that the local flow velocity is the main driver of the erosion distribution. The quantitative profile along the jet centerline, Fig. 5b, shows that the on-axis velocity rises sharply immediately downstream of the needle tip and levels off at about 30.2–30.4 m/s in the fully developed free jet, slightly below the domain maximum found in the narrow annular throat gap.



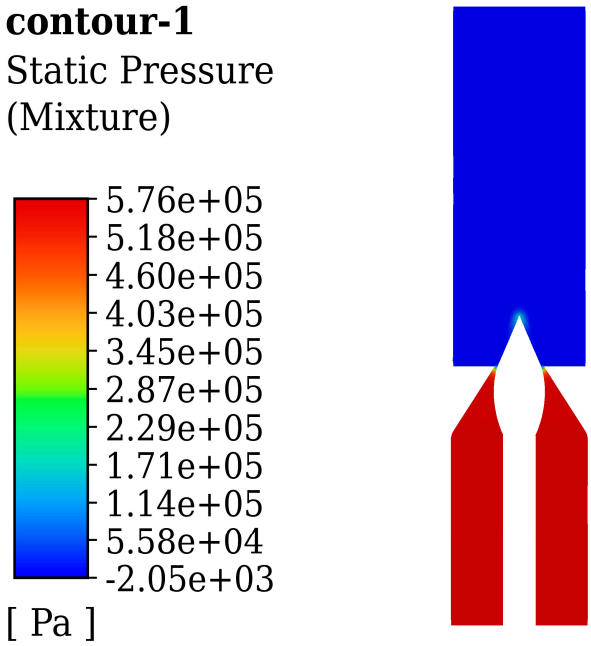
(**a**) Velocity-magnitude contour on the axial mid-plane



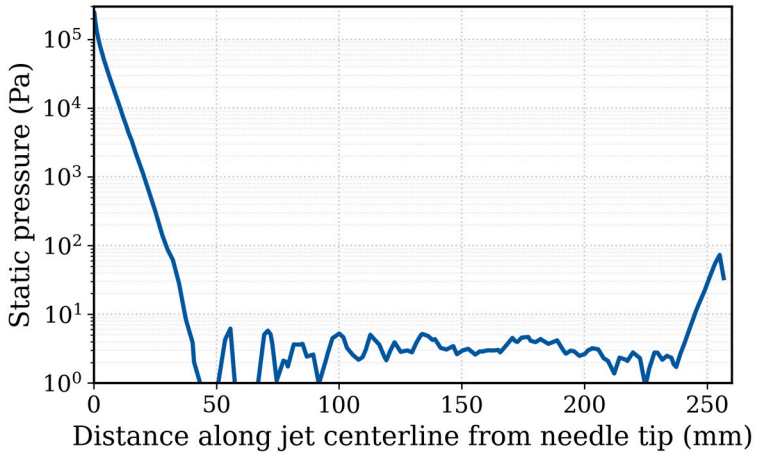
(**b**) Velocity magnitude along the jet centerline

Figure 5: Velocity magnitude of the jet mechanism.

Fig. 6 shows the static-pressure field of the jet mechanism. The area-weighted average inlet pressure is about 563 kPa and decreases rapidly as the flow approaches the nozzle outlet, becoming negative near the outlet, which indicates that most of the pressure energy is converted into kinetic energy at the nozzle outlet. As quantified in Fig. 6b, the on-axis pressure is locally elevated immediately downstream of the needle tip and then collapses, approaching the ambient level within about 40 mm downstream, consistent with the rapid pressure-to-kinetic-energy conversion noted above. Beyond this point the on-axis pressure oscillates within a few pascals of 0—less than 0.05% of the initial value—which reflects the turbulent unsteadiness of the instantaneous flow field (extracted at a single time instant) rather than any physically significant structure.



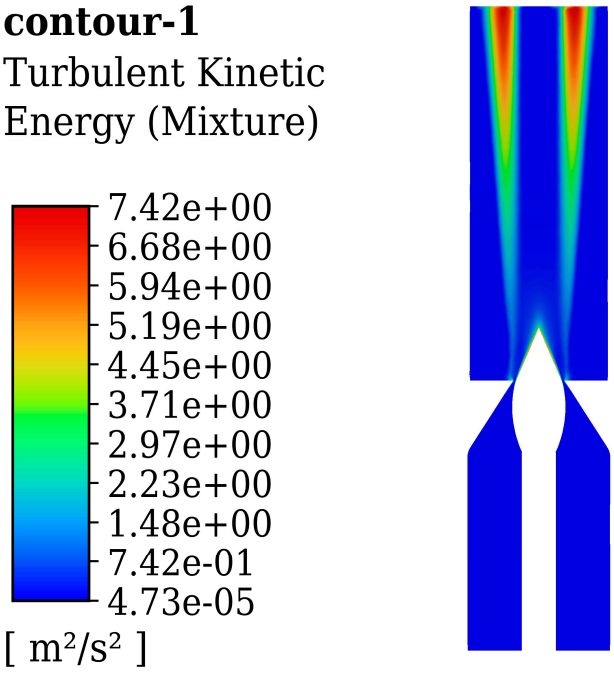
(**a**) Static-pressure contour on the axial mid-plane



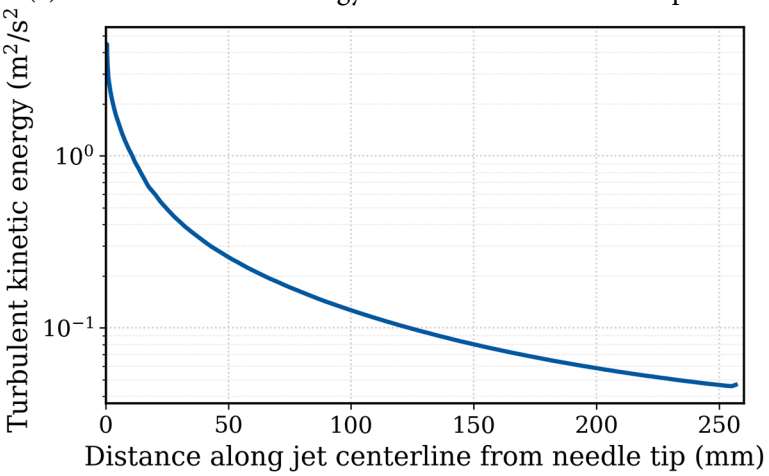
(**b**) Static pressure along the jet centerline

Figure 6: Static pressure of the jet mechanism.

Fig. 7 shows the turbulent-kinetic-energy (TKE) contour. The TKE increases markedly in the jet shear layers downstream of the nozzle outlet and near the needle tip (peak about 7.4 m^2/s^2), reflecting the strong shear and mixing there, where particle–wall collisions are frequent. On the jet centerline, shown in Fig. 7b, the TKE is about 4.1–4.5 m^2/s^2 immediately downstream of the needle tip and decays by roughly two orders of magnitude to about 0.05 m^2/s^2 further downstream, reflecting the dissipation of turbulence as the jet develops away from the needle tip; the larger peak value quoted above occurs off-axis, within the shear layer at the jet boundary.



(**a**) Turbulent-kinetic-energy contour on the axial mid-plane



(**b**) Turbulent kinetic energy along the jet centerline

Figure 7: Turbulent kinetic energy of the jet mechanism.

3.2 The Effect of Particle Diameter on Erosion

To clarify the mechanism behind the non-monotonic dependence of erosion on particle diameter, Fig. 8 compares the sediment-particle trajectories in the jet mechanism for three representative diameters (d = 0.01, 0.1 and 1 mm). For the fine particles (d = 0.01 mm), the low inertia allows the particles to follow the accelerating carrier flow closely; they stay concentrated near the needle surface and are carried onto the needle head and tip, producing the severe tip erosion seen in Figs. 8–10. As the diameter increases to d = 0.1 mm, the growing particle inertia together with the centrifugal effect in the curved accelerating flow throws a large fraction of the particles off the needle tip before impact, so that they cross the annular gap and strike the nozzle inner wall prematurely; the direct loading on the needle tip therefore drops sharply, corresponding to the erosion-rate minimum at d = 0.1 mm. For the coarse particles (d = 1 mm), although

the particles still deviate from the streamlines and collide with the wall prematurely, the kinetic energy carried by each particle is large enough that these off-design impacts still remove wall material effectively, so the overall erosion rate rises again. The trajectory pattern therefore explains why the erosion rate of the jet needle peaks at d = 0.05 mm among the finest particles, drops sharply to a minimum at d = 0.1 mm and then recovers, whereas that of the nozzle first increases, then drops sharply and finally recovers as the particle diameter increases.

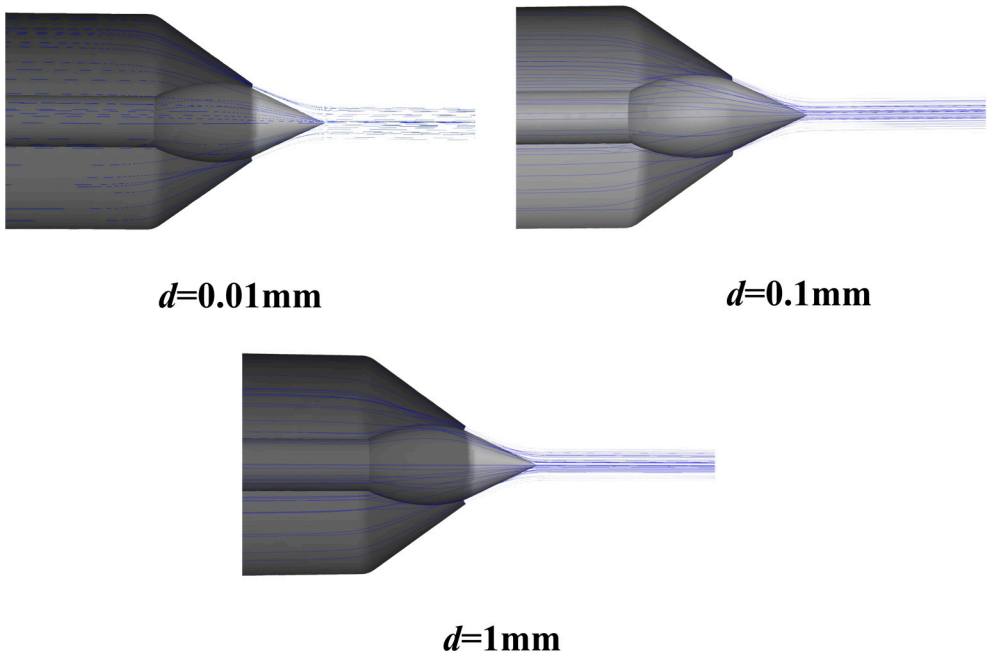


Figure 8: Sediment-particle trajectories in the jet mechanism for different particle diameters.

Fig. 9 shows the erosion contours on the jet-needle surface of the impulse turbine at a sediment volume fraction of 1% for different sediment particle diameters. The jet-needle surface is subjected to non-uniform impacts from high-speed sediment particles, and the erosion is concentrated mainly in the head and tip region. As the sediment particle diameter d increases, the eroded region on the jet-needle surface extends noticeably towards the shank, although the peak erosion rate does not increase monotonically (see Fig. 11). For the fine particles d = 0.01 mm and d = 0.05 mm, erosion of the jet needle is confined to a very small area at the tip; although this eroded area is small, the peak erosion rate there is the highest among all the particle diameters considered (see Fig. 11), with almost no erosion on the needle shank. For the coarse particles d = 0.3 mm and d = 1 mm, the erosion of the jet needle increases significantly. The eroded region is no longer confined to the tip but extends markedly along the needle axis towards the shank, and a continuous annular erosion band of very high intensity develops on the conical transition surface between the needle tip and the shank. The erosion intensity increases progressively from the tip towards the transition zone and peaks on the conical transition surface. At the same time, the erosion on the needle shank becomes increasingly evident as the particle diameter increases. At d = 0.1 mm, the erosion contours show that the eroded region extends slightly towards the shank, but the erosion intensity is markedly lower than for the coarser particles. Overall, the change in the erosion distribution is strongly correlated with the increase in particle diameter.

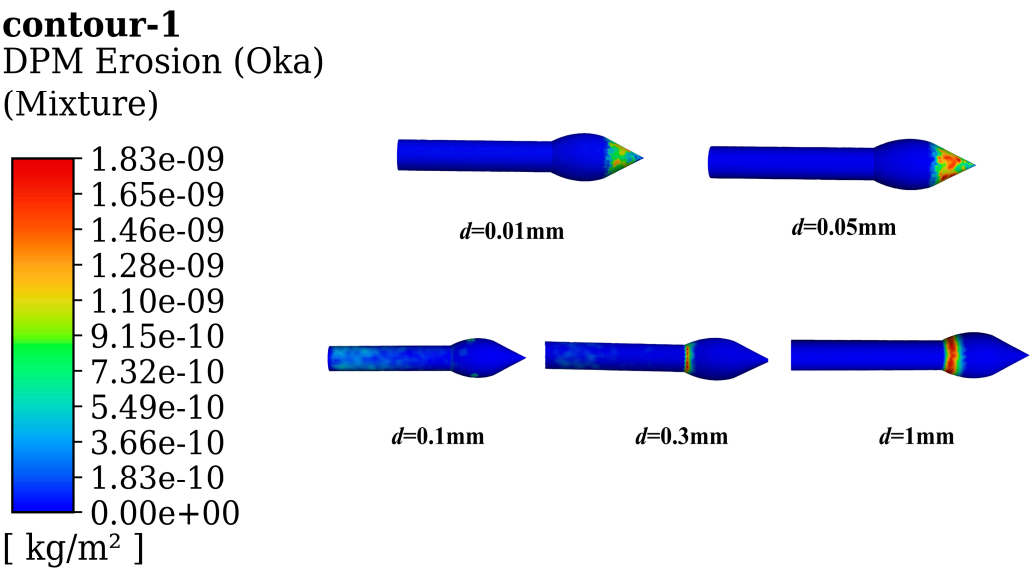


Figure 9: Needle erosion contours at 1% sediment volume fraction with varying particle sizes.

Fig. 10 shows the erosion contours on the inner surface of the nozzle of the impulse turbine at a sediment volume fraction of 1% for different particle diameters. As the sediment particle diameter increases, the overall erosion of the nozzle exhibits a characteristic pattern: it first increases, then drops sharply, and then increases again gradually. For the fine particles d = 0.01 mm and d = 0.05 mm, the erosion of the nozzle surface is very severe; the erosion marks are highly concentrated and relatively evenly distributed, forming a continuous annular erosion zone of very high intensity. When $d \geq 0.1$ mm, the overall erosion of the nozzle drops sharply and the erosion spreads over the entire nozzle surface. In particular, at d = 0.1 mm, the eroded regions are scattered and the overall erosion intensity is much lower than under the fine-particle conditions. As the particle diameter increases further to d = 0.3 mm and d = 1 mm, the erosion of the nozzle flow-passage wall rises slowly again; the eroded zone gradually shifts from the upstream wall towards the outlet throttling edge, forming a new continuous but less severely eroded annular zone at the outlet. Overall, the change in the sediment erosion distribution is correlated with the variation in erosion magnitude and with the increase in particle diameter.

Fig. 11 shows the maximum erosion rates of the nozzle and the jet needle of the jet mechanism at a sediment volume fraction of 1% for different sediment particle diameters. As the particle diameter increases from 0.01 mm to 1 mm, the erosion rate of the jet needle peaks at d = 0.05 mm among the finest particles, drops sharply to a minimum at d = 0.1 mm and then recovers, whereas the erosion rate of the nozzle first increases, then drops sharply, and then increases gradually. For fine sediment (d = 0.01 mm), the erosion rate of the jet needle (5.11×10^{-5} kg·m^{-2}·s^{-1}) is markedly higher than that of the nozzle (1.66×10^{-5} kg·m^{-2}·s^{-1}). Among the diameters considered, the jet-needle erosion rate reaches its overall peak of 6.30×10^{-5} kg·m^{-2}·s^{-1} at d = 0.05 mm, only marginally above the d = 0.01 mm value. The jet-needle erosion rate reaches its minimum of 1.83×10^{-9} kg·m^{-2}·s^{-1} at d = 0.1 mm, whereas the nozzle erosion rate reaches its minimum of 1.63×10^{-9} kg·m^{-2}·s^{-1} at d = 0.3 mm; with a further increase to d = 1 mm the two rates rise again to 1.35×10^{-8} and 2.00×10^{-8} kg·m^{-2}·s^{-1}, respectively. These phenomena occur because the sand-laden water is accelerated to a high velocity through the nozzle constriction. Fine particles have low inertia and follow the flow well, so they strike the head and tip of the jet needle and cause severe erosion there. As the particle diameter increases, the growing centrifugal force throws the particles off the needle tip, so the tip erosion drops sharply (hence the needle minimum at d = 0.1 mm), while many particles collide prematurely with

the inner wall of the nozzle. With a further increase in particle diameter, the kinetic energy of each particle becomes large enough that, even after a premature collision, it still erodes the wall, so the overall erosion rate rises again.

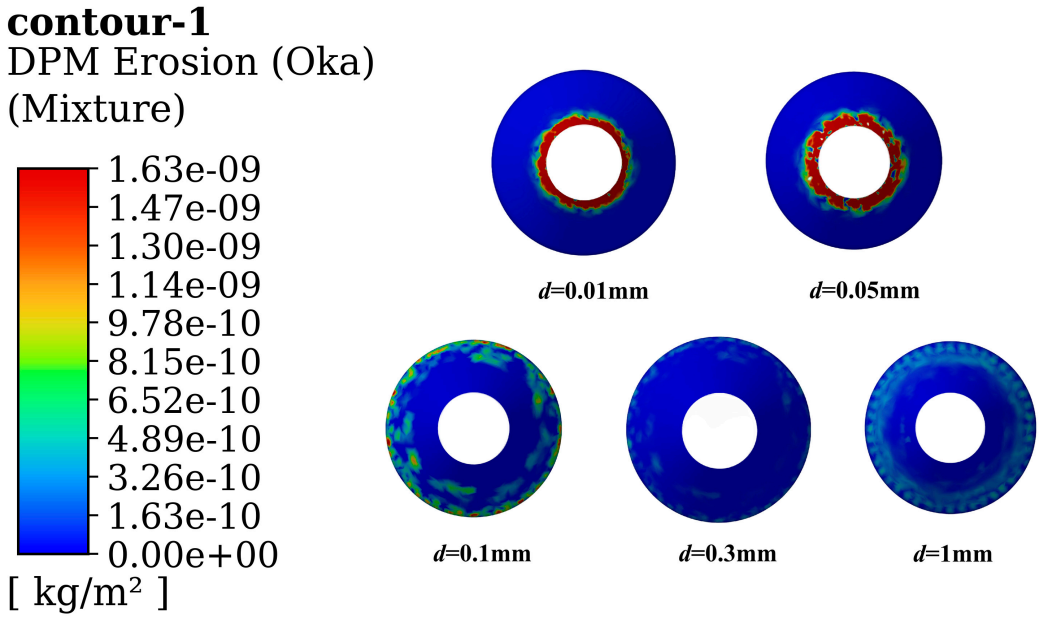


Figure 10: Nozzle erosion contours at 1% sediment volume fraction with varying particle sizes.

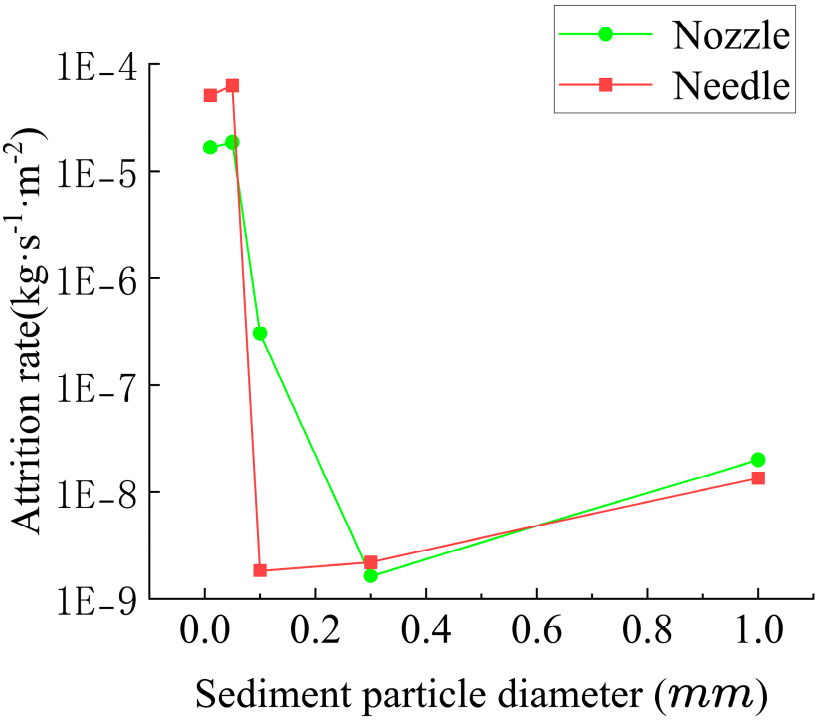


Figure 11: Erosion statistics of jet mechanism at 1% sediment volume fraction and varying particle sizes.

3.3 The Effect of Particle Concentration on Erosion

Fig. 12 shows the erosion distribution on the jet needle of the impulse turbine at a sediment particle diameter of 0.01 mm for various sediment volume fractions, denoted by C_S. In this study, the volume fraction C_S is defined as the ratio of the volume of the sediment particles to the total volume of the mixed fluid (unit: %), and is used to characterize the influence of the solid-phase concentration on erosion.

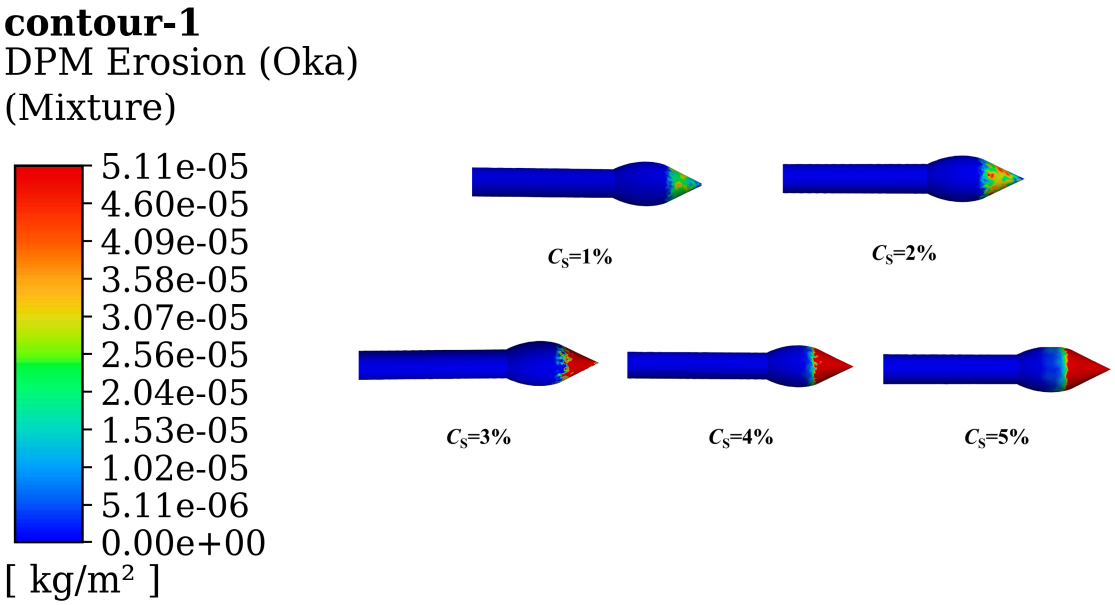


Figure 12: Needle erosion contours at 0.01 mm particle size with varying sediment volume fractions.

As shown in Fig. 12, as the sediment volume fraction increases, the overall erosion of the jet-needle wall rises sharply. The erosion distribution patterns are very similar at different volume fractions, but the erosion intensity differs significantly. Under all operating conditions, the sediment erosion of the jet needle is concentrated in the tip region. The erosion decreases gradually from the needle tip towards the shank, and there is almost no noticeable erosion on the needle shank. At C_S = 1%, only a small area of minor erosion appears at the jet-needle tip, and the overall erosion is low. As C_S increases to 2%, 3%, and 4%, the high-erosion area at the jet-needle tip continues to expand and the erosion intensity keeps rising. When C_S rises to 5%, large areas of severe erosion appear at the jet-needle tip. The reason for this pattern is that, as the volume fraction increases, the number of sediment particles per unit volume of fluid increases significantly. The jet-needle tip is the region in the whole jet mechanism where the flow velocity is highest and the flow is most complex; the sediment particles carried by the high-velocity flow strike the wall of this region directly at very high speed. The frequency of particle–wall collisions increases markedly and the cumulative collision energy keeps intensifying; consequently, the erosion at the jet-needle tip increases sharply as the volume fraction rises, and the high-erosion area gradually extends from the tip towards the shank.

Fig. 13 shows the erosion distribution on the nozzle of the impulse turbine at a sediment particle diameter of 0.01 mm for different sediment volume fractions. As shown in the figure, the most severely eroded part of the nozzle is the annular inner wall at the outlet, where the erosion marks are roughly annular. As the sediment volume fraction increases, the erosion in the annular region at the nozzle outlet also increases. As the flow inside the nozzle accelerates through the constriction, it is concentrated and

ejected at high speed through the annular gap between the jet needle and the nozzle. At the same time, the sediment particles are carried along the inner wall of the nozzle by the high-velocity flow and strike the wall collectively at the outlet, so the erosion marks on the nozzle are mainly annular. In addition, the higher the sediment volume fraction, the greater the number of sediment particles striking the nozzle-outlet wall per unit time, which significantly increases the impact frequency and causes more severe erosion. In particular, when the sediment volume fraction $C_S \leq 2\%$, the sediment erosion is relatively low, with only sporadic minor erosion on the inner wall of the nozzle outlet. When $C_S \geq 3\%$, the sediment erosion increases significantly; the annular erosion zone at the nozzle outlet becomes progressively continuous and its width keeps expanding, and the erosion rises rapidly as the volume fraction increases.

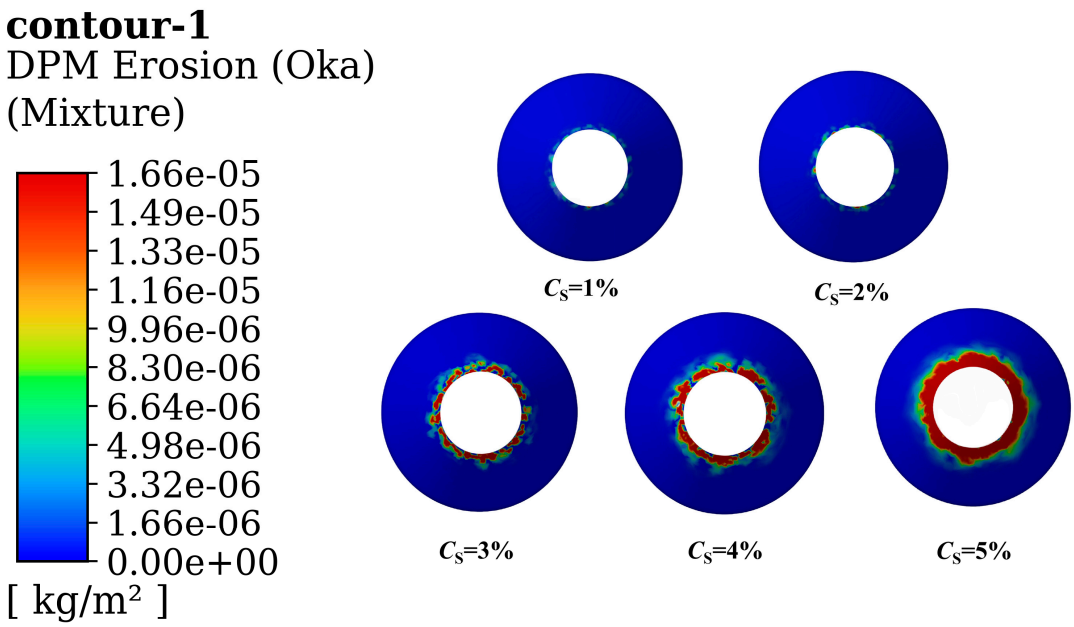


Figure 13: Nozzle erosion contours at 0.01 mm particle size with varying sediment volume fractions.

As shown in Fig. 14, as the sediment volume fraction increases, the erosion rate of the jet-needle wall rises steadily, whereas the erosion rate of the nozzle wall rises overall but dips at C_S = 3% before increasing sharply again. When the concentration increases from 2% to 3%, a substantial number of particles form a "dynamic shield" or "particle curtain" in the near-wall region, which partially mitigates the direct impact of subsequent particles on the wall surface, resulting in a transient decrease in erosion rate. As the concentration continues to rise, this buffering effect is overwhelmed by the intense impact of numerous particles, leading to a sharp resurgence in erosion rate. The erosion rate of the jet-needle wall is consistently higher than that of the nozzle wall, and the difference between the two erosion rates increases gradually as the sediment volume fraction rises. Quantitatively, as the sediment volume fraction increases from 1% to 5%, the maximum erosion rate of the jet needle rises from 5.11×10^{-5} to 1.31×10^{-1} kg·m^{-2}·s^{-1} (about a 2.6×10^{3}-fold increase) and that of the nozzle from 1.66×10^{-5} to 2.86×10^{-3} kg·m^{-2}·s^{-1}, dipping to 1.24×10^{-5} kg·m^{-2}·s^{-1} at C_S = 3% along the way. Because this increase spans more than three orders of magnitude, the dependence of the erosion rate on the sediment volume fraction is approximately exponential rather than linear.

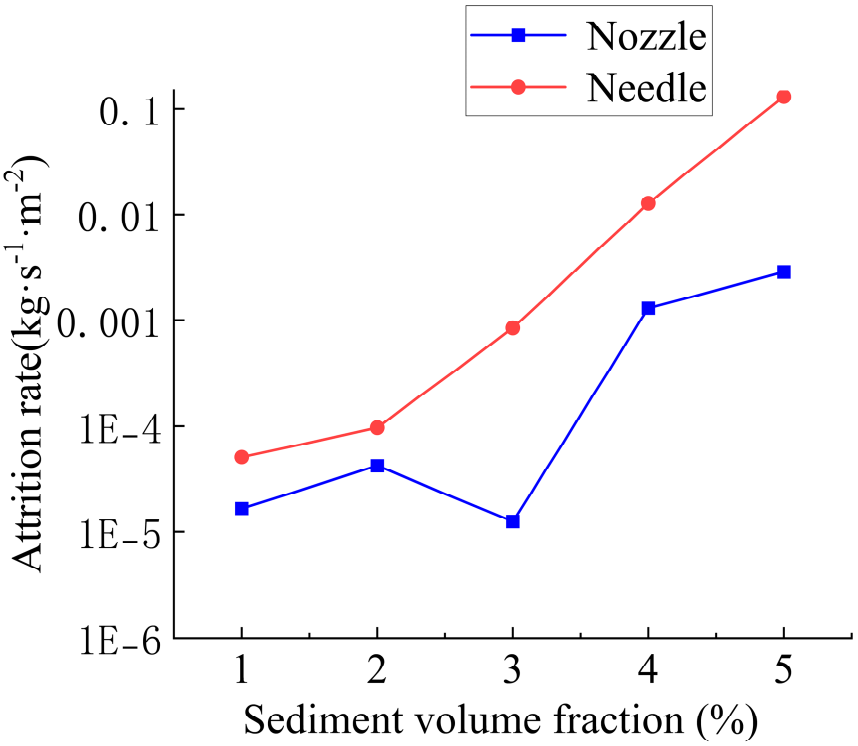


Figure 14: Erosion statistics of jet mechanism at 0.01 mm particle size and varying sediment volume fractions.

3.4 The Effect of Needle Opening on Erosion

In the jet mechanism of an impulse turbine, the needle opening changes the internal flow field and thereby affects the trajectories and impact intensity of the sediment particles. Fig. 15 shows the erosion contours on the jet-needle surface at different needle openings. As shown in the figure, when the high-velocity sand-laden flow passes through the jet mechanism, the sediment particles it carries erode the jet-needle wall. The erosion distribution is markedly non-uniform, being concentrated mainly at the jet-needle tip and the adjacent conical surface, while the needle shank shows almost no particle erosion, with erosion levels close to zero. When the needle opening SR = 0.23, a large area of severe erosion appears at the jet-needle tip, where the erosion is most pronounced. As the needle opening increases from 0.23 to 0.63, the erosion of the jet-needle surface shows a marked and sustained decrease. Not only does the maximum erosion rate keep decreasing, but the high-erosion area also shrinks gradually, with the concentrated-erosion zone narrowing progressively from the entire conical surface of the jet-needle head towards its very tip. When the opening reaches 0.63, the overall erosion improves significantly. This is because, as the needle opening increases, the cross-sectional area of the flow passage increases, which reduces the impact velocity of the flow and the particles; at the same time, the particles strike the needle tip at a shallower, more grazing angle; according to the impact-angle dependence of the Oka model, such impacts remove less material. The combined reduction in impact velocity and impact angle therefore explains the sustained decrease in needle erosion with increasing opening, which is further confirmed by the particle trajectories.

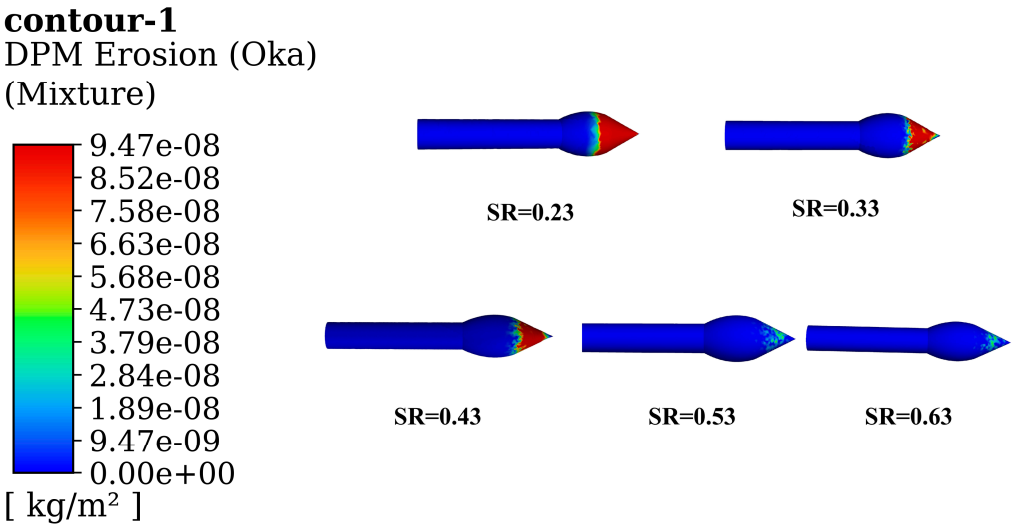


Figure 15: Needle erosion contours under different opening degrees.

Fig. 16 shows the DPM erosion contours on the nozzle wall at different needle openings. As shown in the figure, the erosion on the nozzle is distinctly annular; all eroded areas are concentrated on the inner annular wall near the outlet, while the wall farthest from the outlet shows almost no sign of erosion by sediment particles. When the needle opening SR = 0.23, a continuous, complete high-erosion ring forms on the inner circumference of the nozzle outlet; this is the most severely eroded of all the operating conditions. As the needle opening increases from 0.23 to 0.53, the nozzle erosion rate decreases rapidly. Moreover, the originally continuous band of heavy erosion gradually breaks up into several discontinuous patches, and the eroded area also contracts significantly. When the opening reaches 0.53, only a few scattered, tiny erosion marks remain on the nozzle wall. When the opening is increased further to 0.63, the erosion rises slightly but remains at a relatively low level overall.

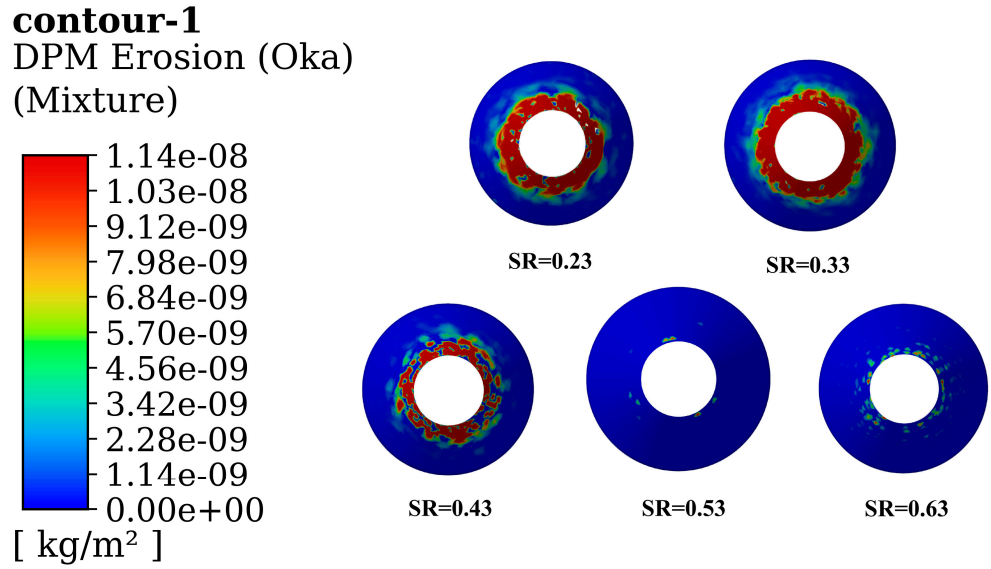


Figure 16: Nozzle erosion contours under different opening degrees.

Fig. 17 shows the statistical erosion results for the jet mechanism at different needle openings. The data show that the erosion rates of both the jet needle and the nozzle generally follow a similar decreasing trend as the needle opening varies; however, there are notable differences in the rates of change and in the actual values over different opening ranges. When the needle opening SR = 0.23, the erosion rates of both the jet needle and the nozzle reach their maxima among all operating conditions, and the erosion rate of the jet needle markedly exceeds that of the nozzle. This indicates that, at small openings, the jet needle is the component of the jet mechanism that suffers the most severe sediment erosion. As the needle opening increases from 0.23 to 0.43, the erosion rates of both components decrease, and the difference between the erosion rates of the jet needle and the nozzle gradually narrows. As the opening increases further from 0.43 to 0.53, the erosion rate of the nozzle decreases sharply, reaching its minimum in this study at SR = 0.53, while the erosion rate of the jet needle continues to decline at a relatively steady rate. When the opening is increased further to 0.63, the erosion rate of the nozzle increases slightly, whereas that of the jet needle continues to decrease gradually. Quantitatively, at SR = 0.23 the maximum erosion rates of the jet needle and the nozzle reach 5.11×10^{-5} and 1.66×10^{-5} kg·m^{-2}·s^{-1}, respectively; the nozzle erosion rate reaches its minimum of 1.14×10^{-8} kg·m^{-2}·s^{-1} at SR = 0.53, and the jet-needle erosion rate decreases further to its minimum of 9.47×10^{-8} kg·m^{-2}·s^{-1} at SR = 0.63.

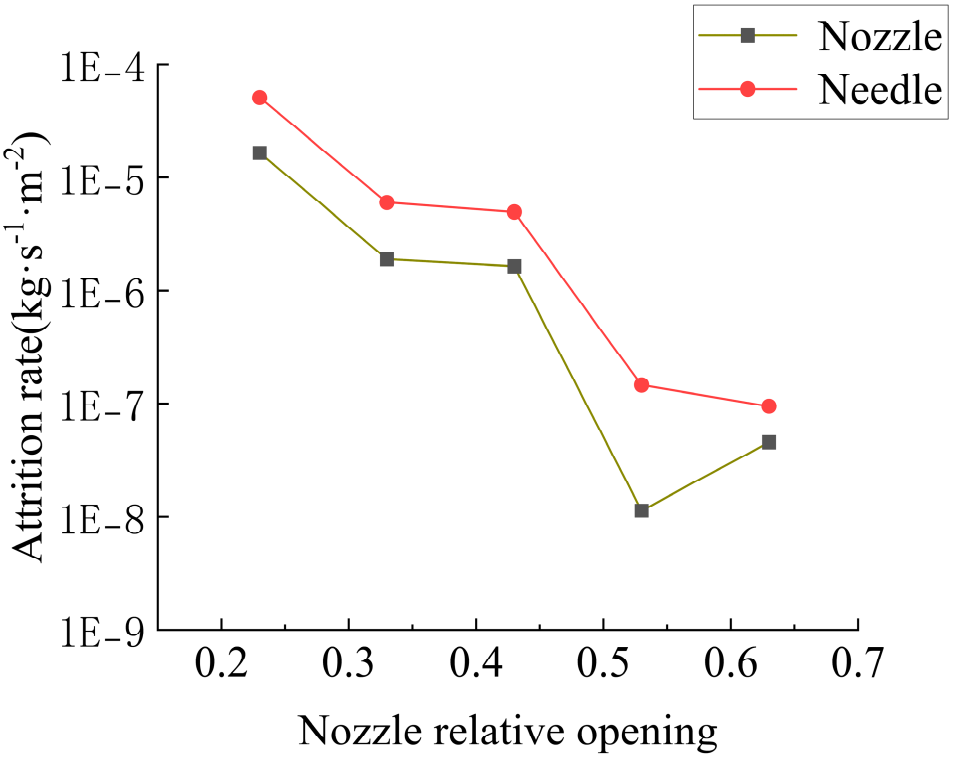


Figure 17: Erosion statistics of jet mechanism under different opening degrees.

To further clarify the mechanism by which the needle opening affects erosion, Fig. 18 compares the sediment-particle trajectories at SR = 0.23 and SR = 0.63. At the small opening (SR = 0.23), the particles remain strongly concentrated and strike the jet-needle tip at a steep angle, producing the severe tip erosion seen above; at the large opening (SR = 0.63), the flow passage widens, so both the impact velocity and

the impact angle at the needle tip decrease and the erosion is markedly reduced. This trajectory pattern explains why the erosion of the jet mechanism decreases as the needle opening increases.

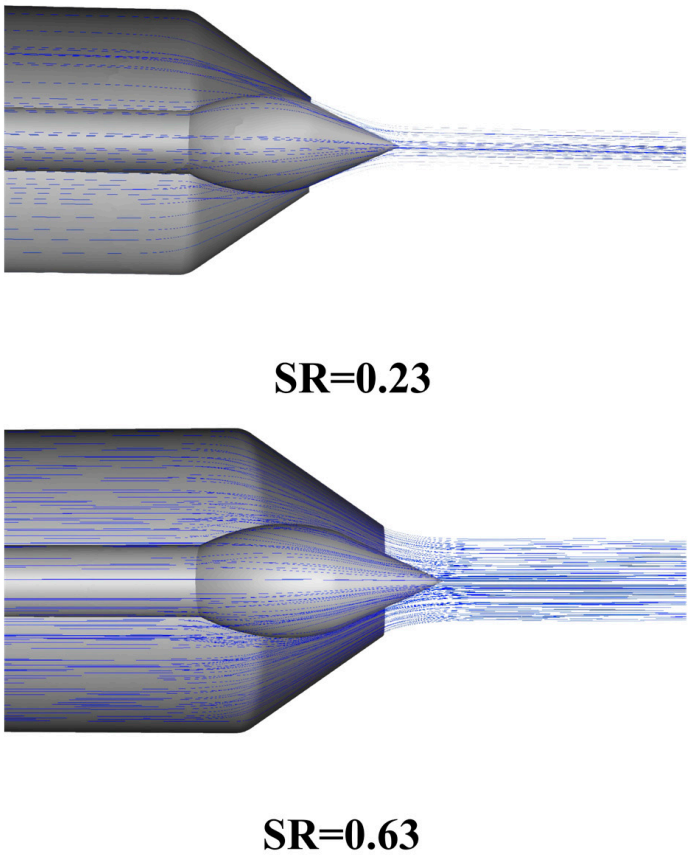


Figure 18: Sediment-particle trajectories in the jet mechanism under different needle openings.

4 Conclusion

In this study, numerical simulations of the water–air–sediment three-phase flow in the jet mechanism of an impulse turbine were carried out using the RNG k-ε turbulence model, the Euler–Lagrange particle-tracking model, and the Oka erosion model, and the erosion characteristics of the flow-passage components were investigated. The effects of the sediment particle diameter, volume fraction, and needle opening on the magnitude and distribution of erosion on the nozzle and the jet needle were analyzed and evaluated. The main conclusions are as follows:

(1) Particle diameter exhibits a non-monotonic influence on erosion. As the diameter increases from 0.01 mm to 1 mm, the eroded area on the jet needle extends from the tip toward the shank, while nozzle erosion first rises, then drops sharply, and finally recovers gradually. Quantitatively, the jet-needle erosion rate peaks at 6.30×10^{-5} kg·m^{-2}·s^{-1} at a diameter of 0.05 mm, falls to a minimum of 1.83×10^{-9} kg·m^{-2}·s^{-1} at 0.1 mm, and then rebounds to 1.35×10^{-8} kg·m^{-2}·s^{-1} at 1 mm. The nozzle erosion rate reaches its lowest value of 1.63×10^{-9} kg·m^{-2}·s^{-1} at 0.3 mm. These results indicate that operating the unit in the low-erosion particle-size range around 0.1–0.3 mm can effectively mitigate wear.

(2) Sediment volume fraction is positively and non-linearly correlated with erosion. When the volume fraction increases from 1% to 5%, the maximum erosion rate of the jet needle surges from 5.11×10^{-5} to 1.31×10^{-1} kg·m^{-2}·s^{-1}, an increase of about 2.6×10^{3} times, and that of the nozzle rises from 1.66×10^{-5} to 2.86×10^{-3} kg·m^{-2}·s^{-1}, though a transient dip occurs at a concentration of 3% due to a particle-shielding effect. Under all conditions, the jet needle consistently suffers more severe erosion than the nozzle. The dependence on concentration is approximately exponential rather than linear, so reducing the sediment volume fraction as much as possible during operation is strongly recommended.

(3) Needle opening is negatively correlated with erosion. At the smallest opening, SR of 0.23, both components experience their highest erosion rates, with the jet needle reaching 5.11×10^{-5} kg·m^{-2}·s^{-1} and the nozzle 1.66×10^{-5} kg·m^{-2}·s^{-1}. As the opening increases to SR of 0.63, the jet-needle erosion rate drops by about 99.8%, while the nozzle erosion reaches its minimum at SR of 0.53 with a value of 1.14×10^{-8} kg·m^{-2}·s^{-1}. Therefore, special attention to tip protection is required when the unit operates at small openings.

(4) For practical operation and maintenance, the following measures are advised: avoid prolonged operation at small needle openings during flood seasons with high sediment loads; apply hardening coatings or protective layers to the jet-needle tip and the annular outlet zone of the nozzle, and increase inspection frequency for these regions; enhance real-time monitoring and adjust operational schedules when the sediment volume fraction exceeds about 3%; and tailor maintenance intervals according to the prevailing particle size and sediment concentration.

While the present study provides useful insights, several limitations should be acknowledged. The sediment particles are treated as monodisperse spheres, the coupling is one-way, the inlet velocity is fixed, and quantitative experimental validation is lacking. Future work should incorporate realistic particle size distributions and non-spherical shapes, adopt two-way coupling with dynamic wall evolution, simulate transient opening processes, and conduct controlled erosion tests to calibrate and validate the model. These enhancements will support more reliable erosion-resistant design and maintenance strategies for impulse turbines in sediment-laden rivers.

Acknowledgement: Not applicable.

Funding Statement: This research was funded by the National Natural Science Foundation of China, grant number 52506041.

Author Contributions: Conceptualization, Dongping Zeng; methodology, Dongping Zeng and Xingyan Chen; software, Xingyan Chen; validation, Xingyan Chen and Yanan Zhao; formal analysis, Dongping Zeng and Shurong Feng; investigation, Dongping Zeng and Fada Zhou; writing—original draft preparation, Shurong Feng and Dongping Zeng; writing—review and editing, Dongping Zeng and Xingyan Chen; supervision, Shurong Feng and Dongping Zeng; funding acquisition, Dongping Zeng and Shurong Feng. All authors reviewed and approved the final version of the manuscript.

Availability of Data and Materials: The authors confirm that the data supporting the findings of this study are available within the article.

Ethics Approval: Not applicable.

Conflicts of Interest: The authors declare no conflicts of interest. Author Shurong Feng and Yanan Zhao are employed by Power China Zhongnan Engineering Corporation Limited. All authors declare that the research was conducted in the absence of any commercial or financial relationships that could be construed as a potential conflict of interest.

Abbreviations

The following abbreviations are used in this manuscript:

C_S	sediment volume fraction (%)
C_V	velocity coefficient (–)
D	nozzle outlet diameter (m)
d	sediment particle diameter (mm)
$E(\alpha)$	erosion rate ($kg \cdot m^{-2} \cdot s^{-1}$)
H_V	Vickers hardness of the wall (GPa)
k	turbulent kinetic energy ($m^2 \cdot s^{-2}$)
S	needle stroke (m)
SR	needle opening, SR = S/D (–)
u	fluid-phase velocity ($m \cdot s^{-1}$)
u_p	particle velocity ($m \cdot s^{-1}$)
α	particle impact angle (°)
ε	turbulent dissipation rate ($m^2 \cdot s^{-3}$)
μ	dynamic viscosity (Pa·s)
ρ	fluid density ($kg \cdot m^{-3}$)
ρ_p	particle density ($kg \cdot m^{-3}$)
RNG	renormalization group
VOF	volume of fluid
DPM	discrete phase model
CFD	computational fluid dynamics
SIMPLEC	Semi-Implicit Method for Pressure-Linked Equations–Consistent

References

1. Li X, Zhou Y, Zhang H, Xiao G, Li Y, Gao Z, et al. Advances in research on impulse hydro-turbine technology. River. 2026;5(1):112–33. [CrossRef].
2. Bajracharya TR, Acharya B, Joshi CB, Saini RP, Dahlhaug OG. Sand erosion of Pelton turbine nozzles and buckets: A case study of Chilime Hydropower Plant. Wear. 2008;264(3–4):177–84. [CrossRef].
3. Rai AK, Kumar A, Staubli T. Hydro-abrasive erosion in Pelton buckets: Classification and field study. Wear. 2017;392–393:8–20. [CrossRef].
4. Shrivastava N, Rai AK. Hydro-abrasive erosion in Pelton turbines: Comprehensive review and future outlook. Renew Sustain Energy Rev. 2025;207:114957. [CrossRef].
5. Ge XF, Sun J, Li Y, Wu D, Zhang L, Hua H. Numerical simulation of silt erosion characteristics of an injector of Pelton turbine. J Hydraul Eng. 2020;51(12):1486–94. (In Chinese). [CrossRef].
6. Sun J, Spinosa P, Messa GV. Analysis of different strategies for the prediction of hydro-abrasive wear in Pelton turbine buckets based on Computational Fluid Dynamics (CFD) simulations. Wear. 2025;570:205954. [CrossRef].
7. Rai AK, Kumar A, Staubli T. Effect of concentration and size of sediments on hydro-abrasive erosion of Pelton turbine. Renew Energy. 2020;145:893–902. [CrossRef].
8. Ge X, Weng X, Zhu W, Yao W, Wang JS. A method for setting the sand outlet of the water distribution ring pipe of an impulse turbine and its effect on sediment wear. Flow Meas Instrum. 2026;110:103312. [CrossRef].
9. Guo T, Liu S, Hu X, Luo Z. Physics of secondary flow phenomenon and erosion characteristics in the injector of a Pelton turbine. Eng Appl Comput Fluid Mech. 2025;19:2479700. [CrossRef].
10. Song X, Wang Z, Bi H, Guo L, Liu Y. Study on the influence of sediment particle size on sediment wear and energy dissipation of impulse turbine nozzles. Energies. 2026;19(12):2800. [CrossRef].
11. Sun J, Sun S, Guo P, Bai J, Fan K. A multi-criteria cavitation erosion risk assessment framework for Pelton turbine buckets under different needle openings. Energy. 2026;361:141665. [CrossRef].
12. Li C, Li F, Guo PC, Sun S, Shen P. Effects of structural parameters of the injector on sediment erosion characteristics in a Pelton turbine. J Hydraul Eng. 2025;56(1):93–105. (In Chinese). [CrossRef].
13. Li C, Li F, Shen P, Guo P. Knowledge discovery of injector geometry effects on Pelton turbine erosion: Approaches for efficient high-head water utilization. Renew Energy. 2025;252:123524. [CrossRef].

14. Chiarelli M, Vetsch DF, Boes RM, Andolfatto L, Münch-Alligné C. On the influence of geometrical parameters and erosive wear on the dynamic behaviour of Pelton turbine runners. Results Eng. 2025;27:105638. [CrossRef].
15. Hu S, Wang X, Huang C, Zhou P, Wang X, Tang L, et al. Transient dynamic characteristics analysis of a prototype Pelton turbine runner based on two-way fluid-structure interaction. Energy. 2026;358:141213. [CrossRef].
16. Yakhot V, Orszag SA. Renormalization group analysis of turbulence. I. Basic theory. J Sci Comput. 1986;1(1):3–51. [CrossRef].
17. Crowe CT, Schwarzkopf JD, Sommerfeld M, Tsuji Y. Multiphase Flows with Droplets and Particles. Boca Raton, FL, USA: CRC Press; 2011. [CrossRef].
18. Schiller L, Naumann A. A drag coefficient correlation. Z Ver Dtsch Ingenieure. 1935;77:318–20.
19. Oka YI, Okamura K, Yoshida T. Practical estimation of erosion damage caused by solid particle impact. Wear. 2005;259(1–6):95–101. [CrossRef].
20. Oka YI, Yoshida T. Practical estimation of erosion damage caused by solid particle impact. Part 2: Mechanical properties of materials directly associated with erosion damage. Wear. 2005;259:102–9. [CrossRef].
21. Vishwakarma R, Pant CS. Field-based characterization and computational assessment of sediment erosion in Pelton turbine injectors at a Himalayan hydropower site. Phys Fluids. 2025;37(9):093315. [CrossRef].
22. Wei XY, Kang XF, Pei J, Wang WQ. Erosion of a micro hydrokinetic turbine considering actual sediment gradation. J Hydraul Res. 2025;63(6):681–95. [CrossRef].